PRAMANA
— journal of
physics

Vol. 79, No. 6
December 2012
pp. 1471–1483

Dynamic imaging and hydrodynamics study of high velocity, laser-accelerated thin foil targets using multiframe optical shadowgraphy

S TRIPATHI, S CHAURASIA, P LESHMA and L J DHARESHWAR*

High Pressure & Synchrotron Radiation Physics Division, Bhabha Atomic Research Centre, Mumbai 400 085, India

*Corresponding author. E-mail: dharesh@barc.gov.in; lj_dhareshwar@yahoo.com

MS received 14 December 2011; revised 16 May 2012; accepted 29 May 2012

Abstract. The main aim of the study of thin target foil–laser interaction experiments is to understand the physics of hydrodynamics of the foil acceleration, which is highly relevant to inertial confinement fusion (ICF). This paper discusses a simple, inexpensive multiframe optical shadowgraphy diagnostics developed for dynamic imaging of high velocity laser-accelerated target foils of different thicknesses. The diagnostic has a spatial and temporal resolution of 12 μm and 500 ps respectively in the measurements. The target velocity is in the range of 10^6–10^7 cm/s. Hydrodynamic efficiency of such targets was measured by energy balance experiments together with the measurement of kinetic energy of the laser-driven targets. Effect of target foil thickness on the hydrodynamics of aluminum foils was studied for determining the optimum conditions for obtaining a directed kinetic energy transfer of the accelerated foil. The diagnostics has also been successfully used to study ablatively accelerated targets of other novel materials.

Keywords. Laser ablation; hydrodynamics; inertial confinement fusion; optical shadowgraphy.

PACS Nos 52.50.JM; 52.50.Lp; 52.25; 52.70

1. Introduction

When a target is irradiated by a high power laser, most of the laser energy is absorbed near the critical surface. Energy then flows towards the ablation surface from where the material is blown off as in a rocket exhaust exerting a thrust on the target to accelerate it in the forward direction. Such laser-ablated and accelerated targets play important roles in the study of target implosion physics of inertial confinement fusion (ICF) [1–3]. Experiments utilizing ablatively accelerated planar targets can model large pellet shells in their early implosion phase. Instead of imploding a pellet, a disk or foil target can be accelerated and treated as a section of a sphere. ICF targets generally have complex structures with layers of different materials to enhance pressure, smoothing of hydrodynamic instabilities etc.

over the cryogenic D-T layer. Studies on hydrodynamics of foil targets can give insights not only about the basic laser–plasma interaction physics, but also, about the generation of the ablation pressure and the shock wave [4–7], hydrodynamic efficiency, energy transfer, growth of instabilities in target motion etc. [8,9]. Studies on simple or more complex structured targets using combination of different materials are therefore of relevance to fusion research. Further, ablative acceleration of target foils to ultra-high velocities can lead to the possibility of generation of extremely high pressures on impact of such foils on matter [10]. Such fast flyers are considered to be one of the most effective types of the ignition drivers for the impact ignition scheme [11,12] in ICF. Several techniques have been adapted to measure foil velocity and acceleration, namely, optical shadowgraphy [13–16] and X-ray backlighting [17,18]. A velocity interferometer system for any reflector coupled with electronic streak camera [19] has been used for the measurement of free surface velocity of laser-shocked and accelerated targets. The more complicated technique of X-ray backlighting is perceived to be more accurate in imaging the dense part of the rear foil. However, Thiell *et al* [20] have shown that the simple technique of optical backlighting with second harmonic or fourth harmonic of the main laser beam can also be used to image the accelerated target rear.

The main diagnostic described in this paper is a novel two-frame optical shadowgraphy set-up with spatial and temporal resolution of 12 μm and 500 ps respectively. The main advantage of this diagnostics is its cost effectiveness. Experiments reported earlier by other authors [16–20] use either optical or X-ray framing cameras. These optoelectronic instruments are extremely expensive. In their case, delay between the frames or the frame capture rate (in commercial cameras, this is about 10^6 Hz) depends on the speed setting of the instrument. Frame exposure times are in the range of a few tens of picoseconds to hundreds of picoseconds. In our set-up, we have shown that similar studies on ablatively accelerated targets can be successfully done, without sacrificing on resolution, with CCD cameras which are very much less expensive compared to commercial framing cameras. Also, there is an added advantage of flexibility and independent setting of delay between the two frames captured. The frame capture rate in our set-up can be as high as 10^9 per second since the minimum delay between the two probe pulses is about 1 ns. Frame exposure time here is set by the laser pulse duration of 500 ps. However, the same set-up can yield an exposure time of a few picoseconds where the laser used is based on chirped pulse amplification technique.

2. Experiments

The experiments were conducted using the laser system developed at the High Pressure and Synchrotron Radiation Physics Division, Bhabha Atomic Research Centre, India [21]. The main Nd:Glass laser system for this purpose is indigenously developed and delivers a laser pulse with a maximum energy of 20 J on the target. Laser pulse can be varied from 300 to 800 ps. This pulsed-single shot laser system consists of a commercial laser oscillator with an output energy of 100 mJ per pulse which is amplified through a chain of linear amplifiers to increase the laser pulse energy. The final laser beam is focussed with a 50 cm focal length, $f/5$ plano-convex lens on the target to a 100 μm diameter spot, to produce maximum intensity of 5×10^{14} W/cm^2. The laser pulse has a peak

to background contrast of 10^5. The intensity of the pre-pulse is thus $<10^9$ W/cm^2 and cannot generate a pre-plasma from the target, before the arrival of the main pulse. The experimental laser–plasma chamber is equipped with a remotely controlled target mount and is evacuated to a pressure of 10^{-6} Torr.

The two-frame optical shadowgraphy set-up uses a second harmonic backlighting probe beam. This probe is derived by extracting 1% of the laser light from the main beam at the final stage by introducing a beam splitter BS1 as shown in the schematic experimental set-up in figure 1. Synchronization of the time of arrival of the main beam on the target and probe beam can be adjusted by the delay introduced by the mirrors M3 and M4 in the main laser beam. An appropriate delay is introduced in the probe beam path to record shadowgrams of the target at any desired instant of time with respect to the main laser beam. This has been achieved with the help of an optical delay comprising of mirrors M6, M7 and a prism. Further, for obtaining two frames at two different delays per laser shot, this beam is split into two parts by BS2. One of the beams is propagated through a half-wave plate (HWP). In the other beam, an optical delay is introduced with the help of mirrors M8 and M9. Thus, two orthogonally polarized probe beams are generated for the two shadowgram frames at two different delays. A polarizing beam splitter P is used to recombine these two beams after introducing the delay between them, generating two collinearly propagating optical probe pulses arriving at two different instants at the target. All optical components are mounted on translational stages to afford an easy and independent variation in the delay between the two pulses. These probe pulses then pass through the KD*P crystal and get converted to second harmonic (532 nm) for shadowgraphy. After this, the two probe pulses are split again into two beams with the help of another polarizing beam splitter P and recorded with the cameras CCD1 and CCD2 to generate the two frames. The scheme of irradiation of the target by the main laser beam and the two probe beams is shown in the inset of figure 1.

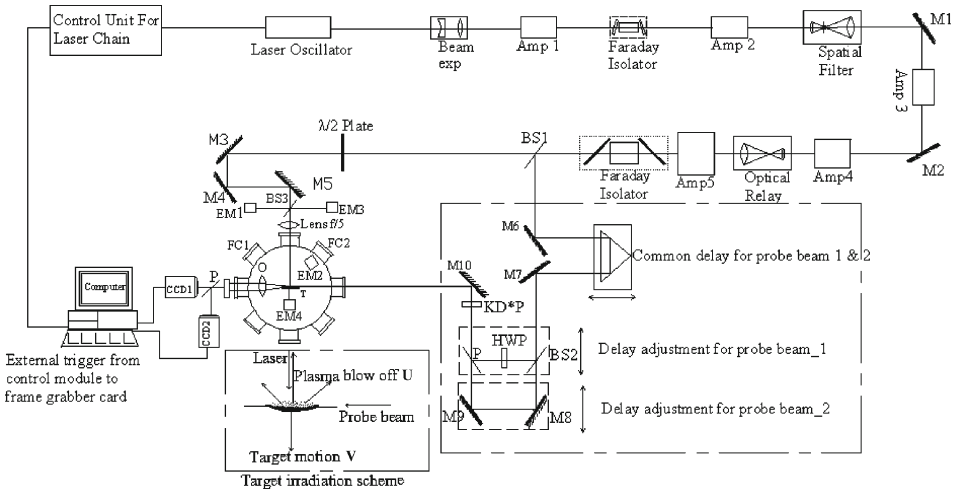

Figure 1. Schematic of the experimental set-up for the multiframe optical shadowgraphy diagnostic. Inset shows the target irradiation scheme by the main pulse and the two probe pulses.

Thus, in the present set-up, per laser shot, we can fix two delays between the two frames. For a subsequent laser shot, a constant delay can be introduced in both the arms by changing the delay in the main delay arm using the prism mounted on translation stage. The delay between the main laser pulse and the two probe pulses thus can be smoothly and continuously varied from 2 to 10 ns by simple adjustment of optical components of the delay arm. The optical delay between the different beams, that is, the main laser beam and the two probe beams, is accurately measured with an optical streak camera having a temporal resolution of 20 ps and also using a vacuum biplanar photodiode (rise time-80 ps) and a Tektronix 2.5 GS/s oscilloscope as shown in figures 2a and b respectively.

The accelerated portion of the target is imaged by an $f/2$ objective lens O onto the CCD cameras with an overall magnification of 3.48. The spatial resolution of the imaging set-up which depends on the optical quality of the probe beam and the components used is observed to be 12 μm as measured by illuminating an air force test pattern (supplied by Ms. Melles Griot) by the probe beam. Temporal resolution is limited by the exposure time or the probe pulse duration. It can be further improved by shortening the probe pulse by some other standard techniques.

The angular distribution of the ions and velocity of the front plasma blow-off are measured using ion diagnostics which are based on time-of-flight methods using ion collectors. The two ion collectors FC1 and FC2 are placed at 55° (Θ_1) and 46° (Θ_2) with respect to the target normal. FC1 ion collector is placed at a distance of 53.21 cm and FC2 at 73.21 cm from the point of irradiation on the target surface as shown in figure 1. Typical ion signal plot for the 2, 5 and 10 μm thick aluminum foils is shown in figure 3. The sharp peak is the photopeak due to X-rays from the plasma which designates the time marker. Average ion velocity U, which is also the plasma ablation velocity, is measured by dividing the distance of the ion collector from the target by the time-of-flight (time duration between the photopeak and the peak of the ion signal). If U_1 and U_2 are the ion velocities measured by FC1 and FC2, considering a $\cos^n\Theta$ distribution of ions [22] about the target normal, we can write

$$U_1 = U\cos^n\Theta_1 \quad \text{and} \quad U_2 = U\cos^n\Theta_2$$

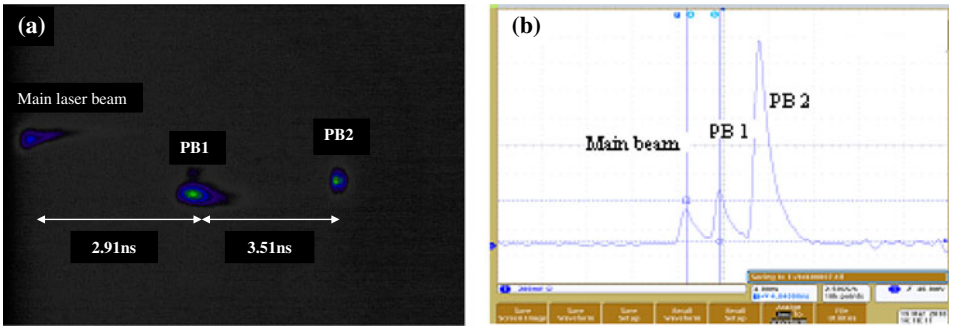

Figure 2. (**a**) Optical streak camera record of the main laser pulse and the two probe pulses to measure the optical delay between them. (**b**) Oscilloscope (2.5 GS/s) signal of a fraction of the main laser pulse and the two probe pulses, measured by a fast biplanar detector.

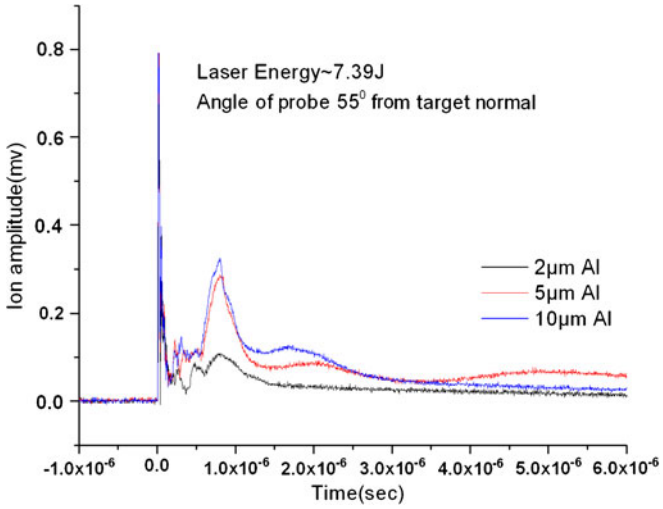

Figure 3. Typical ion detector signal detected by FC1 and FC2.

where U is the ion velocity in a direction normal to the target and Θ is the angle between the ion collector and the normal to the target. Experimental measurement of U_1 and U_2 can give us the value of n from the equation

$$n = \log \frac{(U_1/U_2)}{\log(\cos\Theta_1/\cos\Theta_2)}. \tag{1}$$

Using the value of n from (1), U, the plasma ablation velocity is measured for determining the hydrodynamic efficiency as elaborated in §3.2.

3. Results and discussions

3.1 *Hydrodynamics of aluminum foils of different thicknesses*

Optical shadowgrams recorded for 0.8, 2, 5 and 10 μm thick aluminum target foils at varying delays are shown in figure 4. The shadowgram on top shows an undisturbed target foil before being irradiated by the laser beam. Direction of the incident laser beam is indicated by the arrow on the left-hand side. These photographs show the target movement at different time instants.

It is clearly visible that 10 and 5 μm thick target foils exhibit a smooth motion with uniform profile on the target rear whereas the 2 μm foil shows the presence of hydrodynamic instabilities at larger delays. The growth of such instabilities leads to an unstable foil motion at a delay of 8.3 ns. The 0.8 μm foil is observed to be unstable right from the first shadowgram, which is the early phase of target motion.

The graph of maximum foil movement in the forward axial direction (parallel to the laser beam) vs. the delay of the probe beam is shown in figure 5. The graphs have been plotted for 2, 5 and 10 μm thick foils, which had stable motion. The error bars in this figure are obtained from the spatial and temporal resolutions of the experimental

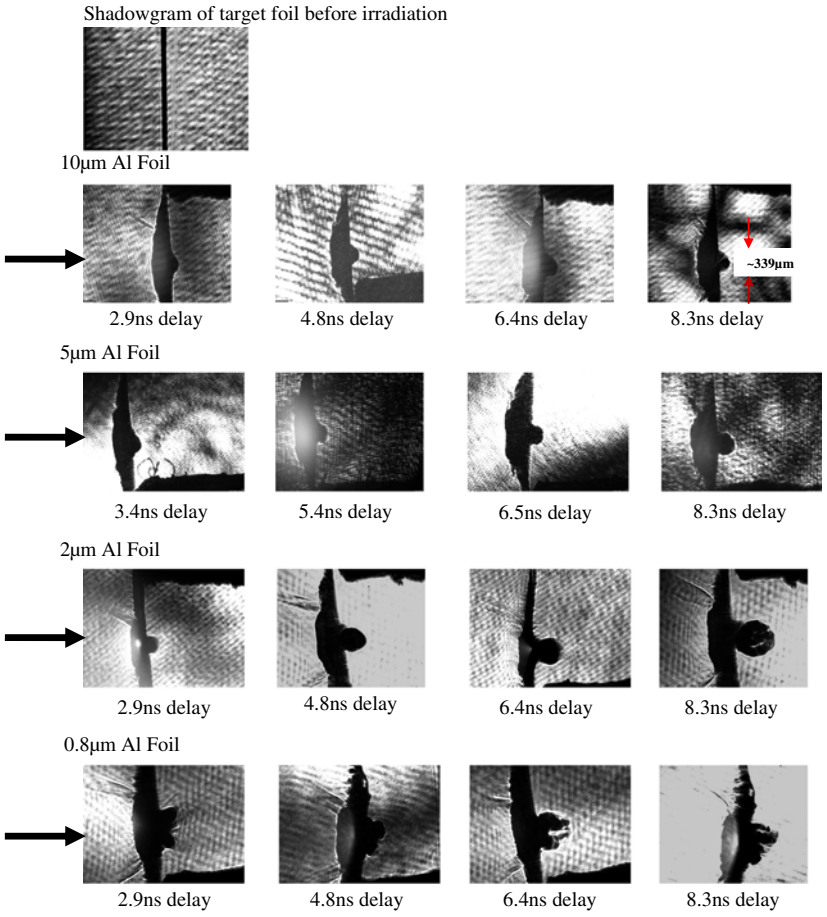

Figure 4. Optical shadowgrams for 0.8, 2, 5 and 10 μm thick aluminum target foils at different probe delays at an incident laser intensity of 1.8×10^{14} W/cm^2.

set-up. Slope of the linear fit to these experimental points gives the target foil velocity V. Target motion for the 0.8 μm thick target could not be ascertained due to the growth of instabilities leading to target break up.

The scaling of the foil velocity with respect to the laser intensity is given by the expression $V \propto I^{\kappa}$. Variation of target foil velocity with incident laser intensity is shown in figure 6. The scaling exponents from these graphs are observed to be in the range of 0.53 to 0.56. These values agree well with the analytical models given by other authors [23,24], based on momentum conservation. Their results indicate that the foil velocity scales with the laser intensity with a scaling exponent κ which varies between 0.5 and 0.7.

Success of impact ignition as mentioned earlier relies on the transfer of kinetic energy of the accelerated foil on a pre-compressed fusion target. Transfer of kinetic energy therefore is maximized for directed, one-dimensional motion of the laser-accelerated foil. The

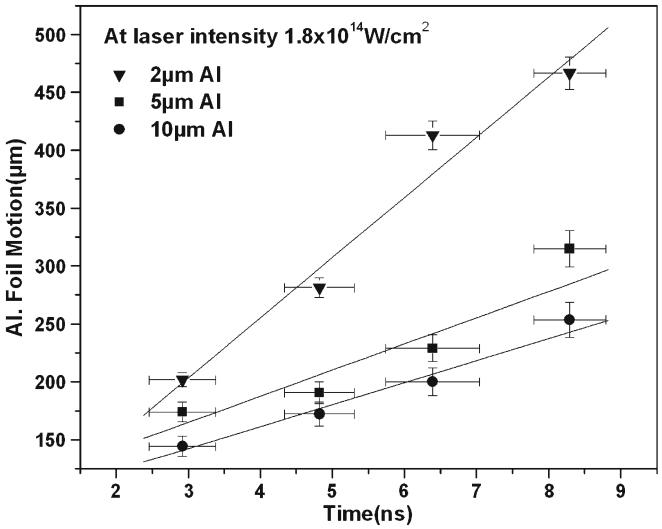

Figure 5. Graph of rear foil movement vs. the probe delay for different target foils. Slope of the graphs gives the target foil velocity as: 2 μm – 5.19 $\times$ 10^6 cm/s, 5 μm – 2.23 $\times$ 10^6 cm/s and 10 μm – 1.17 $\times$ 10^6 cm/s.

kinetic energy (KE) carried by the accelerated target foil depends on its mass and velocity and can be calculated using the simple expression

$$\mathrm{KE} = \frac{1}{2}\, mV^2 = \frac{1}{2}(\pi D^2/4)\rho t V^2\ 10^{-7}\,\mathrm{J}, \tag{2}$$

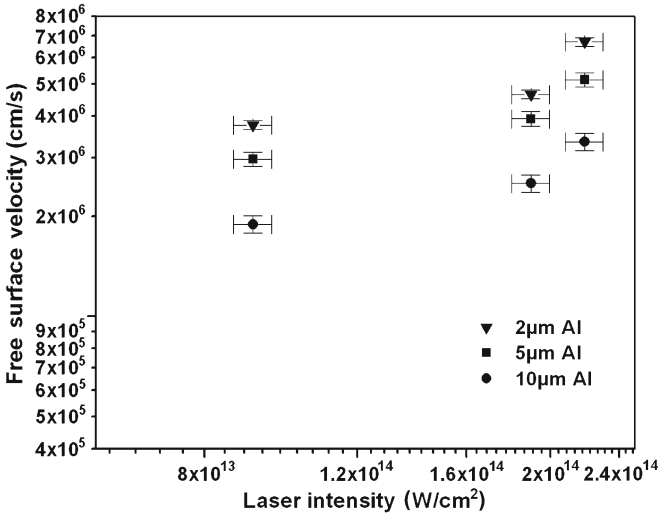

Figure 6. Scaling of target foil velocity with laser intensity. Scaling exponents for 2, 5 and 10 μm foils are: 0.537, 0.546 and 0.564 respectively.

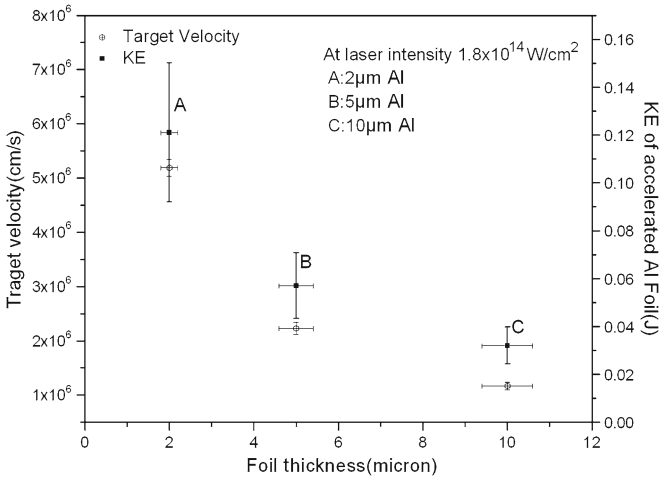

Figure 7. Variation of velocity and kinetic energy of the accelerated target foil, for different thicknesses at an incident laser intensity of 1.8×10^{14} W/cm^2.

where m is the mass, V is the velocity, D is the diameter of the laser spot on the target, ρ is the density and t is the thickness of the accelerated foil (all in CGS units). Kinetic energy carried by the target foil, at the early part of the acceleration phase can be calculated by substituting the values of parameters in the above expression, for different aluminum foils. Figure 7 shows the variation of target velocity and kinetic energy of the accelerated target foil, for different target foil thicknesses at a laser intensity of 1.8×10^{14} W/cm^2. It is observed that KE decreases with the foil thickness. Even though thicker foils carry a higher accelerated mass, KE drops due to the quadratic dependence on foil velocity.

3.2 *Hydrodynamic model*

The hydrodynamics of an ablatively accelerated target foil has been generally explained by considering a one-dimensional model described by Ripin *et al* [24]. This rocket analogy is used to describe the hydrodynamic behaviour of the target during the acceleration phase. In this case, the target (rocket) of mass M and velocity V is accelerated by the steady-state blow-off (exhaust) of the plasma (propellant) at a constant velocity U defined in the accelerated target (rocket) frame of reference. At any given time, the rate of change of momentum of the target is

$$\frac{\mathrm{d}(MV)}{\mathrm{d}t} = -\frac{\mathrm{d}M}{\mathrm{d}t}(U - V). \tag{3}$$

Or equivalently,

$$M\frac{\mathrm{d}V}{\mathrm{d}t} = -U\frac{\mathrm{d}M}{\mathrm{d}t}. \tag{4}$$

Equation (4) is integrated to yield the final mass M and velocity V of the target as a function of the plasma blow-off velocity U and initial mass M_0 giving

$$\frac{V}{U} = \ln\left(\frac{M_0}{M}\right). \tag{5}$$

Equation (5) applies to the case of steady-state laser-driven ablation. Hydrodynamic calculation and experiments have shown that a steady-state ablation, with a well-defined ablation velocity U, is set-up within the first nanosecond of the interaction [25]. For small mass losses eq. (5) reduces to

$$\frac{V}{U} \approx \frac{\Delta M}{M_0}, \tag{6}$$

where $\Delta M = M_0 - M$ is the ablated mass.

The hydrodynamic conversion efficiency, defined as the final target kinetic energy divided by absorbed laser energy, can be derived from eq. (5) and the conservation of energy. The rate of absorption of laser energy, $\dot{E}_\mathrm{a}$ must be balanced by the energy dissipated in the ablation and acceleration of the target. Assuming negligible radiation losses,

$$\dot{E}_\mathrm{a} = \frac{\mathrm{d}}{\mathrm{d}t}\left(\frac{1}{2}MV^2\right) + \frac{1}{2}(-\dot{M})\,(U-V)^2\,. \tag{7}$$

Note again that in a steady-state situation, the continuity equation allows us to use the asymptotic ion ablation velocity U in (7). The asymptotic velocity is the blow-off velocity remote from the target, where most of the internal energy has been converted into kinetic energy of expansion. Using eq. (4), eq. (7) reduces to

$$\dot{E}_\mathrm{a} = -\frac{1}{2}U^2\frac{\mathrm{d}M}{\mathrm{d}t}. \tag{8}$$

Equation (8) can now be integrated to give

$$E_\mathrm{a} = \frac{1}{2}U^2\,(M_0 - M)\,, \tag{9}$$

where E_a is the absorbed laser energy.

Hydrodynamic efficiency, η_h, is an important parameter that gives the fraction of the laser energy input, which goes into the hydrodynamic motion of the target. The hydrodynamic conversion efficiency is therefore defined as the ratio of the kinetic energy of the ablatively accelerated target foil to the absorbed laser energy.

$$\eta_\mathrm{h} = \frac{1}{2}\left(\frac{MV^2}{E_\mathrm{a}}\right). \tag{10}$$

Using (9) and (5) in (10), we then obtain simply

$$\eta_\mathrm{h} = \frac{(V/U)^2}{[\exp(V/U) - 1]}. \tag{11}$$

For small mass losses, this reduces to

$$\eta_\mathrm{h} \sim \frac{V}{U} \sim \frac{\Delta M}{M_0}. \tag{12}$$

Table 1. Summary of laser energy balance and hydrodynamic efficiency for aluminum foil targets of different thicknesses.

Target	2 μm Al	5 μm Al	10 μm Al
Transmitted energy (mJ)	31.58	3.00	56.23
Scattered energy (mJ)	4459.89	5466.97	3596.69
Back-reflected energy (mJ)	435.46	348.37	348.37
Incident energy (J)	7.39	7.39	7.39
Absorbed energy (J)	2.46	1.57	3.39
Target kinetic energy (J)	0.121	0.057	0.032
Hydrodynamic efficiency (η_h)	5%	3.7%	1%

η_h was measured in our experiments by two methods. In eq. (10), target kinetic energy was calculated knowing the target velocity determined from the optical shadowgrams, using the expression given in eq. (2). In the early phase of target acceleration, the diameter of the accelerated part of the target can be considered equal to the laser irradiation spot on the target. The thickness t of the accelerated target is accurately determined by calculating the ablation thickness using expression (6). It is observed that the thickness of the accelerated target foil is almost equal to the thickness of the original foil since ΔM is very small compared to original target foil mass. The absorbed laser energy was experimentally determined using energy balance measurements. Energy meters were used to measure the scattered, back-reflected and transmitted laser energy as shown schematically in figure 1. A 4% beam splitter followed by two energy meters (EM1 and EM3) were used to measure incident and back-reflected laser energy. Scattered energy was measured by EM2 and integrated over 2π. Transmitted laser energy was detected by EM4. Table 1 shows the measured values of these parameters and hydrodynamic efficiency η_h for the three foil thicknesses.

Ion velocity measured by FC1 and FC2, calculated values of n from (1) and η_h from eq. (12) for different targets are given in table 2. The values of η_h obtained using eqs (10) and (12) are observed to match well. These values are also agreeing with the results in [26] and [23].

Table 2. Summary of front plasma blow-off ion velocity calculation and hydrodynamic efficiency. T1, T2 in seconds and U_1, U_2, U in cm/s.

Target	T1(FC_1)	T2(FC_2)	$U_1 = r_1/T_1$	$U_2 = r_2/T_2$	Log (U_1/U_2)	n	$\cos^n\Theta_1$	$U = U_1 \cos^n\Theta_1$	$\eta_h = V/U$
2 μm Al	7.97E-7	9.83E-7	6.68E7	7.447E7	−0.047	0.5353	0.7426	8.995E7	0.057 (5.7%)
5 μm Al	7.912E-7	1.07E-6	6.7252E7	6.842E7	−0.0074	0.0842	0.9543	7.047E7	0.032 (3.2%)
10 μm Al	7.912E-7	1.07E-6	6.7252E7	6.842E7	−0.0074	0.0842	0.9543	7.047E7	0.017 (1.7%)

3.3 *Effect of target density on target foil hydrodynamics*

The versatility of the optical shadowgraphy set-up is established by using it to perform interesting experiments on hydrodynamics of novel targets. Simple metal foil targets (Cu, Au, Bi), layered targets (Al+Au, plastic+Al or Au; plastic with an overlayer of metal nanoparticles) as well as low-density foams of carbon, polymer and bismuth have been studied. As an example of a novel target, we present briefly some of the interesting findings with bismuth metal foams of density 100 mg/cm^3 (super-critical density). At the laser wavelength of 1.06 μm, the critical plasma density up to which the laser can penetrate is about 3 mg/cm^3. Foam layers are recommended for ICF targets for enhancing laser absorption and to reduce beam structure imprint on laser-driven targets [27–29], as well as for increasing conversion efficiency to soft X-rays [30,31]. They have also been found capable of mitigating the effect of hydrodynamic instability growth. However, in these foams having a 3D network of submicron fibres, several authors have reported that the laser beam can penetrate to large depths and thus heating of the target takes place over a larger volume [32–34]. Hydrodynamic energy losses are observed to be lower and the total mass ablated is higher. Shadowgrams in figures 8a–c are recorded for targets with bismuth foam having a density of 100 mg/cm^3 and thickness of 30 μm, at three different delays. Figures 8d–f are for the solid bismuth target of density 9.78 g/cm^3. The shadowgrams clearly show a decrease in the lateral dimension of the plasma on the front side for a solid compared to the low-density foam. Lateral dimension of the plasma plume in the foam target is observed to be about 1300 μm at a probe delay of 4.8 ns. Plasma diameter is almost half the size for solid bismuth. Focal spot diameter in these experiments was 100 μm. This is a direct consequence of the enhanced lateral energy

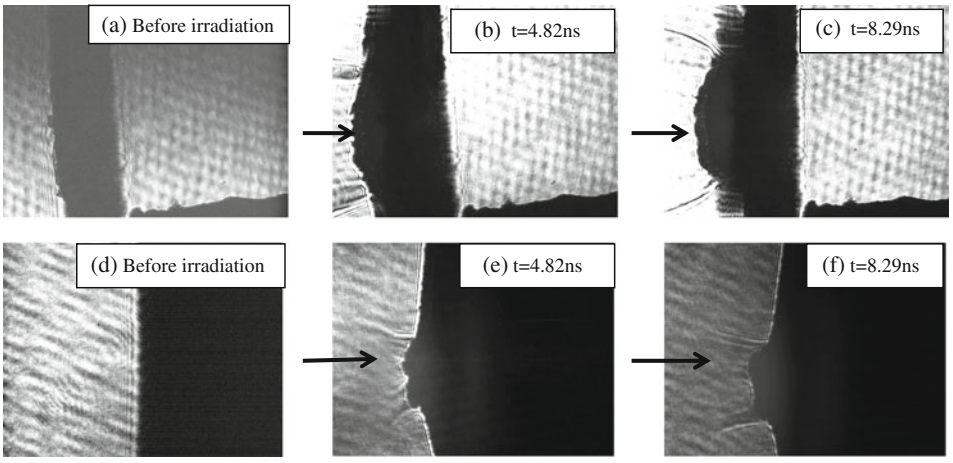

Figure 8. **(a, b, c)** Shadowgrams recorded for bismuth foam target of 100 mg/cm^3 density and 30 μm thickness. **(d, e, f)** are for a solid bismuth target of density 9.78 g/cm^3. **(a)**, **(d)** are the images of targets before irradiation by the main laser beam. **(b)**, **(e)** are recorded for a probe delay of 4.8 ns and **(c)**, **(f)** for a probe delay of 8.2 ns.

transport in case of such low-density foam targets. The volume of the heated low-density hot corona is observed to be larger by a factor of 1.78 for the foam target than for the solid one. We have also reported a 15% enhancement in soft X-ray (0.7–1.56 keV range) emission in bismuth foam targets compared to solid bismuth [35,36].

4. Conclusion

A simple diagnostic, namely, two-frame optical shadowgraphy technique has been set-up to measure the target velocity of laser-ablated and accelerated thin aluminum targets of varying thicknesses. The spatial and temporal resolution of the diagnostics is 12 μm and 500 ps respectively. The velocity of 2, 5 and 10 μm thick aluminum foil targets at a laser intensity of 1.8×10^{14} W/cm^2 is in the range (5–6) $\times 10^6$ cm/s. The velocity is observed to scale with laser intensity as I^{κ} where $\kappa = 0.53$–0.57. The kinetic energy carried by these laser-accelerated foils is in the range of 0.03 to 0.1 J. Energy balance experiments were done to measure absorbed laser energy and thus the hydrodynamic efficiency η_{h}. The values of η_{h} are 1–5% which agree with the hydrodynamic models. This agreement has shown the accuracy of the diagnostics and confirmed the fact that it can be used for any other target. Many novel targets were studied using this multiframe optical shadowgraphy diagnostics. Some of the interesting features of laser-ablated, low-density bismuth foam targets are presented.

Acknowledgements

The authors wish to acknowledge the support and continuous encouragement received from S M Sharma, Head, HP&SRD and S Kailas, Director, Physics Group, BARC. Authors wish to acknowledge excellent support provided by C G Murali and D S Munda for the smooth laser operation and also acknowledge N Borisenko and her group from Lebedev Physical Institute, Moscow, for providing us the bismuth foam targets.

References

[1] J Knuckles, L Wood, A Thiessen and G Zimmerman, *Nature* **239**, 139 (1972)
[2] S E Bodner, *J. Fus. Energy* **1**, 221 (1981)
[3] B Canaud, S Laffite and M Temporal, *Nucl. Fus*. **51**, 62011 (2011)
P B Radha *et al*, *IEEE Trans. Plasma Science* **39**, 1007 (2011)
[4] R J Trainer *et al*, *Phys. Fluids* **25**, 1989 (1982)
[5] R Cauble *et al*, *Phys. Rev. Lett*. **70**, 2102 (1993)
[6] G Collins, P Celliers, L Da Silva *et al*, *Phys. Plasmas* **5**, 1864 (1998)
[7] P M Nilson, S P D Mangles, L Willingale *et al*, *Phys. Rev. Lett*. **103**, 255001 (2009)
[8] V A Samalyuk, O Sadot, R Betti *et al*, *Phys. Plasmas* **13**, 056312 (2006)
[9] J Lindl, *Phys. Plasmas* **2**, 3933 (1995)
[10] H Azechi *et al*, *Plasma. Phys. Contr. Fusion* **47**, B815 (2005)
[11] M Murakami and H Nagatomo, *Nucl. Instrum. Methods. Phys. Res*. **A544**, 67 (2005)
[12] J Badziak *et al*, *Appl. Phys. Lett*. **92**, 211502 (2008)
[13] L J Dhareshwar *et al*, *Pramana – J. Phys*. **25**, 63 (1985)

[14] L J Dhareshwar *et al*, *Plasma Phys. Control. Fusion* **3**, 165 (1993)
L J Dhareshwar, N Gopi, C G Murali *et al*, *Shock Waves* **14**, 231 (2005)
[15] L J Dhareshwar, N K Gupta, S Chaurasia *et al*, *IoP J. Phys*. (*Proceeding of Fifth International Conference on Inertial Fusion Sciences and Applications, 2009*), **244**, 22018 (2010)
[16] J Badziak *et al*, *Appl. Phys. Lett*. **91**, 081502 (2007)
[17] A Raven, H Azechi, T Yamanaka and C Yamanaka, *Phys. Rev. Lett*. **47**, 1049 (1981)
[18] J Grun, S P Obenschain, B H Ripin, R R Whitlock, E A McLean, J Gardner and J A Stamper, *Phys. Fluids* **26**, 588 (1983)
[19] P M Celliers, G W Collins, L B Da Silva, D M Gold and R Cauble, *Appl. Phys. Lett*. **73**, 1320 (1998)
E Moshe, E Dekel, Z Henis and S Eliezer, *Appl. Phys. Lett*. **69**, 1379 (1996)
[20] G Thiell, B Meyer, P Aussage and X Fortin, *Opt. Commun*. **46**, 305 (1983)
[21] S Chaurasia, D S Munda, C G Murali, N K Gupta and L J Dhareshwar, BARC Report No. BARC/2008/E/006, 2008
[22] E Woryna, P Parys, J Wolowski and W Mroz, *Laser. Part. Beams* **14**, 293 (1996)
[23] B H Ripin, R R Whitlock, F C Young, S P Obenschain, E A McLean and R DeCoste, *Phys. Rev. Lett*. **43**, 350 (1979)
[24] B H Ripin, R DeCoste, S P Obenschain *et al*, *Phys. Fluids* **23**, 1012 (1980)
[25] M K Matzen and R L Morse, *Phys. Fluids* **22**, 654 (1979)
[26] K Eidmann, F Amiranoff, R Fedosejevs, A G M Maaswinkel, R Petsch, R Siegel and S Witkowski, *Phys. Rev*. **A30**, 2568 (1984)
[27] Yan Hu *et al*, *Phys. Plasmas* **18**, 053301 (2011)
[28] S Yu Guskov *et al*, *Laser. Part. Beams*. **18**, 1 (2000)
[29] M Desselberger *et al*, *Phys. Rev. Lett*. **74**, 2961 (1995)
[30] S Chaurasia, S Tripathi, D S Munda, G Mishra, C G Murali, N K Gupta, L J Dhareshwar, A K Rossall, G J Tallents, Rashmi Singh, D K Kohli and R K Khardekar, *Pramana – J. Phys*. **75**, 1191 (2010)
[31] N G Borisenko, S Chaurasia and L J Dhareshwar, 7th *International Conf. Inertial Fusion Science and Applications* (Bordeaux, France, 2011)
[32] S V Bondarenko *et al*, *Quantum Electron*. **31**, 39 (2001)
[33] S Yu Guskov *et al*, *Quantum Electron*. **27**, 696 (1997)
[34] D Hoarty *et al*, *Phys. Plasmas* **6**, 2171 (1999)
[35] S Tripathi, S Chaurasia *et al*, *AIP Conf. Proceedings* **1313**, 236 (2010)
[36] S Chaurasia, N G Borisenko, P Leshma, A Orekhov, S Tripathi, A I Gromov, D S Munda and L J Dhareshwar, 25th *National Symp. on Plasma Science and Technology, IASST* (Guwahati, India, 2010)